Robotica (2011) volume 29, pp. 903–915. © Cambridge University Press 2011
doi:10.1017/S0263574711000117

Driving force analysis for the secondary adjustable system in FAST

Zhu-Feng Shao, Xiaoqiang Tang*, Xu Chen and Li-Ping Wang

Institute of Manufacturing Engineering, Department of Precision Instruments and Mechanology, Tsinghua University, Beijing 100084, P.R. China

(Received in Final Form: January 29, 2011. First published online: February 22, 2011)

SUMMARY

The Secondary Adjustable System (SAS) addressed here is a central component of the Five-hundred-meter Aperture Spherical radio Telescope (FAST). It is a 6-degree-of-freedom rigid Stewart manipulator, in which one platform (the end-effector) should be controlled to track-desired trajectory when another platform (denoted as the base) is moving. Driving force analysis of the SAS is the basis for selecting rational servomotors and guaranteeing the dynamic performance, which will affect the terminal pose accuracy of the FAST. In order to determine the driving forces of the SAS, using the Newton–Euler method, the inverse dynamics of the Stewart manipulator is modeled by considering the motion of the base. Compared with the traditional dynamic models, the inverse dynamic model introduced here possesses an inherent wider application range. By adopting the kinematic and dynamic parameters of the FAST prototype, the driving force analysis of the SAS is carried out, and the driving force optimization strategies are proposed. Calculation and analysis presented in the paper reveal that there are three main factors affecting the driving forces of the SAS. In addition, the driving force analysis of this paper lays out guidelines for the design and control of the FAST prototype, as well as the structure and trajectory optimization.

KEYWORDS: Newton–Euler method; Stewart manipulator; Inverse dynamics; Inverse kinematics; FAST.

1. Introduction

The large telescope (LT), also known as the square kilometer array, is first proposed at the General Assembly of the International Union of Radio Science (URSI) in 1993. In 1994, Chinese astronomers carried out the conceptual design of the Five-hundred-meter Aperture Spherical radio Telescope (FAST), which will be located in the Karst region of Guizhou Province, southwest of China. With the joint efforts of Chinese astronomers and engineers, the layout design of the FAST has already been accomplished.[1,2]

A typical radio telescope is composed of a reflector and a receiver. However, owing to the large aperture, the mechanism design of the FAST, as shown in Fig. 1, has the following two outstanding features:

* Corresponding author. E-mail: tang-xq@mail.tsinghua.edu.cn

(1) *The active main reflector*. The reflector, divided into 4000 small elements, can correct spherical aberration to achieve full polarization and a wide reflect band. The diameter of the active main reflector is 520 m.
(2) *Feed support system*. The system consists of three parts, which are a cable-driven Stewart manipulator, an A–B rotator and a rigid Stewart manipulator. The rigid Stewart manipulator is actually the Secondary Adjustable System (SAS) and is our study object. The A–B rotator and the SAS are mounted in the feed cabin, as shown in Fig. 2.

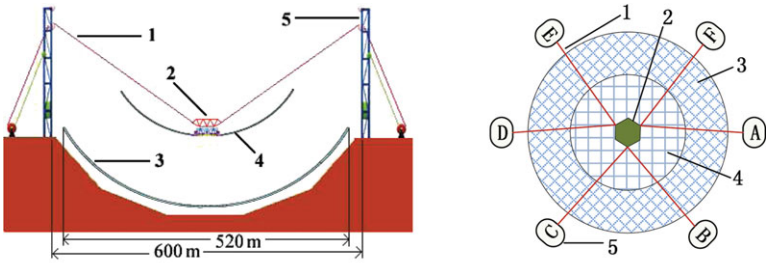
These three parts of the feed support system are arranged in series. The top of the A–B rotator is connected with the end-effector of the cable-driven Stewart manipulator, while the bottom is linked to the base of the rigid Stewart manipulator, i.e., the SAS. Receivers are attached to the end-effector of the SAS, as shown in Fig. 2.

The feed support system is a typical macro/micro manipulator system, which is usually composed of a large (macro) robot carrying a small (micro) high precession robot such as a parallel manipulator. The small high performance manipulator charges for local operation, while retains the high speed and large work space of a bigger robot.[3] In FAST, the cable-driven Stewart manipulator and the A–B rotator, which constitute the hybrid macro robot, provide a wide range of translation and rotation, called the First Support System (FSS) in FAST. The SAS is in charge of compensating the terminal trajectory error, to achieve the terminal pointing accuracy of 8″ and the terminal positioning accuracy of 10 mm, as required.

As the micro robot, the dynamic performance of the SAS affects the overall performance of the FAST. In addition, the driving force analysis of the SAS is the basis for selecting rational servomotors and guaranteeing the dynamic performance. Thus, the analysis of both the driving force and the optimization strategies, which are the focus of this paper, are inevitable for the design, check, and control of the SAS in FAST.

As shown in Fig. 2, the SAS is a typical Stewart parallel manipulator.[4] It is a 6-degree-of-freedom (DOF) parallel manipulator with two bodies (the end-effector and the base) connected together by six extensible limbs. Each limb, which is connected with the base by a universal joint at one end and the end-effector by a spherical joint at the other, is driven by either a hydraulic cylinder or a set of servomotor and lead screw. Owing to the closed-loop

https://doi.org/10.1017/S0263574711000117 Published online by Cambridge University Press



(a) Front view. (b) Top view.

Fig. 1. Sketch map of the FAST. 1: Cable-driven Stewart manipulator (six cable limbs are indicated by red lines, while the base is defined by six cable-connection points in towers A, B, C, D, E, and F). 2: Feed cabin. 3: Active main reflector. 4: Focus surface (trace surface of receivers). 5: Tower (illustrated by six capitals from A to F).

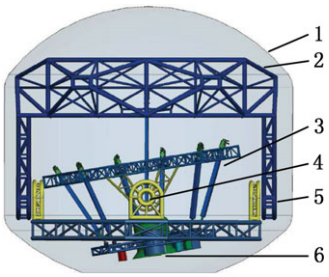


Fig. 2. Sketch map of the feed cabin. 1: Protection shield. 2: End-effector of the cable-driven Stewart manipulator. 3: Rigid Stewart manipulator (SAS). 4: *A*-axis of the A–B rotator. 5: *B*-axis of the A–B rotator. 6: Receivers.

architecture, parallel manipulators have potentials of high rigidity, high acceleration, high accuracy, and high load-carrying capacity over traditional serial manipulators.[5] In addition, parallel manipulators possess the capacity of answering the increasing needs of industry in terms of high-speed machining and automation.[6] This statement can be justified by various successful applications of Stewart manipulators. With the rapid development of industrial computer and parallel mechanism theory, applications of the Stewart manipulator expand to various fields, such as medical equipment, processing equipment, and so on. Stewart manipulators are widely used as simulators, especially aircraft simulators.[7,8] Other important applications are high-precision machining tools and high-precision positioning platforms.[9–11] In addition, these are also extensively used as vibration isolation platforms.[12,13] Currently, these have shown potentials in astronomy, as presented in ref. [2].

Obviously, the inverse dynamics of the parallel manipulator is fundamental to any analysis of the driving force. However, the dynamic modeling of the parallel manipulator is inherent complicated in contrast to that of the traditional serial manipulator. In order to obtain the dynamics of parallel manipulators, many studies have been carried out. The Stewart platform, known as the most classic one, attracts great attention. Based on different mechanical principles, several methods can be adopted to establish the rigid body dynamic model of the parallel manipulator, such as the Newton–Euler method,[14–17] the Lagrangian formulation,[18–20] the principle of virtual work,[21–24] and the Kane method.[25,26] The Newton–Euler formulation is concluded as an approach with clear physical meaning.

Most work in the inverse dynamics field of the parallel manipulator focuses on the manipulator with stable base. The inverse dynamic modeling of the SAS involves the Stewart manipulator with a moving base. So the modeling procedure in this paper is deduced under non-inertia frames. As the motion of the base is considered, the inverse dynamic model deduced in this paper possesses a wider range of application.

The remainder of this paper is organized as follows. In the next section, the rigid Stewart parallel manipulator studied here is described in detail. The algebraic expressions of both inverse dynamics and kinematics of the Stewart manipulator with a moving base are deduced in Section 3. The simulation procedure of dynamic equations in the MATLAB software is illustrated in Section 4. Section 5 deals with the driving force analysis. The driving force optimization strategies are discussed in Section 6. Finally, conclusions of this paper are given in Section 7.

2. System Description

As shown in Fig. 3, the study object is a 6-DOF Stewart parallel manipulator. Each limb is connected with both the base by a universal joint and the end-effector by a spherical joint. Then, there is no rotation along each limb. As demonstrated in Fig. 3, let $\{\boldsymbol{B}\}$ be the base frame $o' - x'y'z'$, attached to the geometric center of the base with the x'-axis crossing B_1B_6 at the midpoint, and the z'-axis perpendicular to the SAS base plane. Let $\{\boldsymbol{P}\}$ be the end-effector frame $o - xyz$, attached to the geometric center of the SAS end-effector with the y-axis crossing P_1P_6 at the midpoint, and the z-axis perpendicular to the end-effector plane. The global frame $\{\boldsymbol{G}\}$ is a translational non-inertia frame $O - XYZ$, which reflects the translational of the end-effector of the cable-driven Stewart manipulator. It is attached to the intersection of two revolution axes of the A–B rotator, with the X-axis along the A-axis of the A–B rotator and the Z-axis along the opposite direction of gravity. The ground frame $\{\boldsymbol{I}\}$ is an inertia coordinate system $O' - X'Y'Z'$, attached to the ground. Besides, the global frame $\{\boldsymbol{G}\}$ always parallels with the inertia frame $\{\boldsymbol{I}\}$. All frames mentioned above are right-handed coordinate systems.

At initial state of the feed support system, rotation angles of the A–B rotator are zero, which means that the end-effector of the cable-driven Stewart manipulator is parallel to the base of the SAS. The three axes, i.e., the Z-axis, the z-axis, and the z'-axis are collinear, along the opposite direction of the

https://doi.org/10.1017/S0263574711000117 Published online by Cambridge University Press

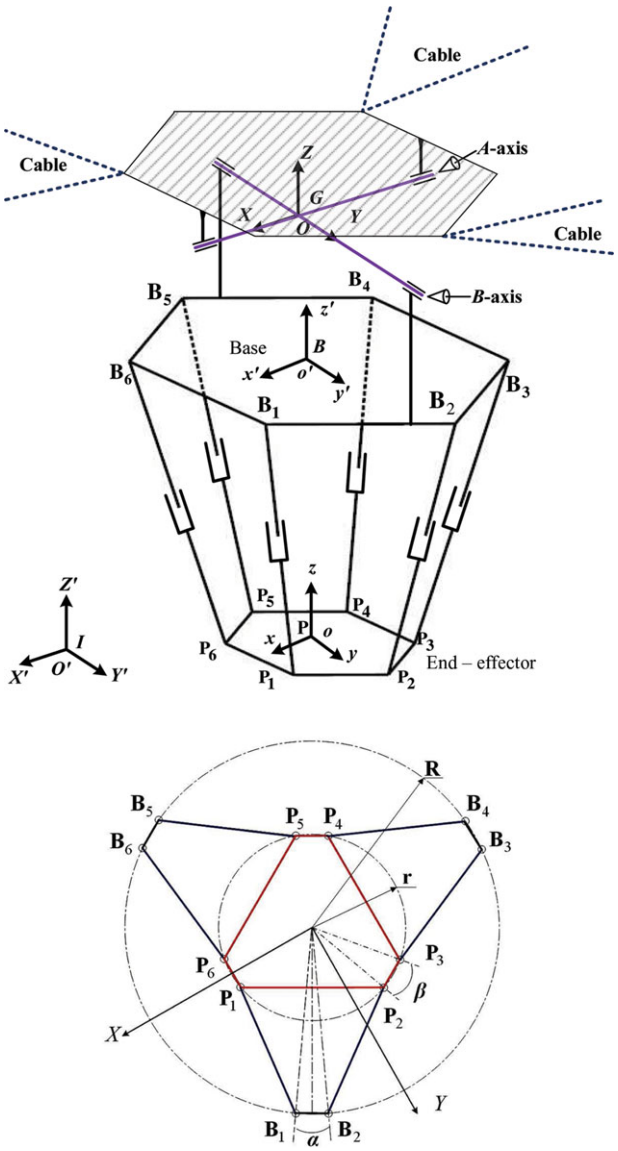


Fig. 3. Kinematic model of the SAS. (a) Isometric drawing of the SAS and the A–B rotator. (b) Top view of the SAS.

gravity, with the X-axis, and Y-axis along the A-axis and B-axis, respectively. The initial distance between the SAS base and the SAS end-effector is 3.3 m.

The notations that have been used in this paper are shown in Table I. Other symbols have been described at the place of first appearance. Generally, vectors and matrices are described in boldface, while leg numbers are denoted by subscripts. The left superscripts of symbols show the coordinate systems, under which physical quantities are described.

3. Dynamic Equations

In the first part of this section, the kinematics of both a single limb and the SAS end-effector are described. In the second part, the inverse dynamics of the SAS is derived through the Newton and Euler equations of limbs and the end-effector. Considering that the SAS base is attached to the moving macro robot (the cable-driven Stewart manipulator and the A–B rotator), the dynamic equations are derived in global frame $\{\boldsymbol{G}\}$. As a result, the kinematic and dynamic parameters required in kinematic and dynamic equations are all transformed in $\{\boldsymbol{G}\}$. All SAS variables except the kinematic variables of the end-effector pertain to an arbitrary limb. So, the limb index $i$can be neglected for convenience.

3.1. Kinematics

The kinematic model of an SAS limb is shown in Fig. 4. Two local reference frames denoted as $\{\boldsymbol{L}\}$ and $\{\boldsymbol{U}\}$ are established. Frame L is attached to the base point B (the rotation center of the universal joint of the limb), with the x-axis along the limb. Theoretically, orientation of the y-axis of frame L can be determined by the cross production of x-axis and an arbitrary vector, which must not parallel x-axis. In this paper, location vector of the base point is used to determine the y-axis of frame L. Then, the z-axis is easy to obtain by the cross production of x-axis and y-axis in $\{\boldsymbol{B}\}$. Frame U is attached to end-effector point P (the rotation center of the spherical joint of the leg), and parallel to the frame L. The

Table I. Notation description.

Symbol	Physical meaning	In frame
$\boldsymbol{k}$	Position of the intersection of the A–B rotator	Base
${}^{\mathrm{G}}\boldsymbol{R}_{\mathrm{B}}$	Rotation matrix. Orientation of the SAS base	Global
$\boldsymbol{t}$	Position of the SAS end-effector	Base
${}^{B}\boldsymbol{R}_{\mathrm{P}}$	Rotation matrix. Orientation of the SAS end-effector	Base
${}^{\mathrm{G}}\boldsymbol{\omega}_{\mathrm{B}}$	Angle velocity of the SAS base	Global
${}^{\mathrm{G}}\boldsymbol{\varepsilon}_{\mathrm{B}}$	Angle acceleration of the SAS base	Global
${}^{\mathrm{B}}\boldsymbol{\varepsilon}_{\mathrm{P}}$	Angle acceleration of the SAS end-effector	Base
${}^{\mathrm{B}}\boldsymbol{\omega}_{\mathrm{P}}$	Angle velocity of the SAS end-effector	Base
$\boldsymbol{b}$	Position vector of the SAS base point	Base
$\boldsymbol{p}$	Position vector of the SAS end-effector point	End-effector
$\boldsymbol{a}$	Acceleration of the global frame	Inertial
$\boldsymbol{a}_{\mathrm{U}}$	Accelerations of mass center of the upper part in SAS limb	$\{\boldsymbol{L}'\}$
$\boldsymbol{a}_{\mathrm{L}}$	Accelerations of mass center of the lower part in SAS limb	$\{\boldsymbol{L}'\}$
$\boldsymbol{a}_{\mathrm{Lr}}$	Translational acceleration of $\{\boldsymbol{L}'\}$	$\{\boldsymbol{I}\}$
$\boldsymbol{a}_{\mathrm{P}}$	Accelerations of mass center of the SAS end-effector	$\{\boldsymbol{P}'\}$
$\boldsymbol{a}_{\mathrm{Pr}}$	Translational acceleration of $\{\boldsymbol{P}'\}$	$\{\boldsymbol{I}\}$

https://doi.org/10.1017/S0263574711000117 Published online by Cambridge University Press

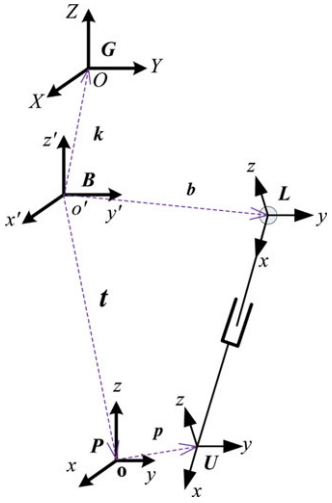


Fig. 4. Kinematic model of a SAS limb.

kinematic and dynamic parameters will be transformed to $\{\boldsymbol{G}\}$ or $\{\boldsymbol{L}'\}$ and $\{\boldsymbol{P}'\}$ (non-inertial translational frames, not shown in the Fig. 3), which are parallel to $\{\boldsymbol{G}\}$ attached to base point B and the geometrical center of the SAS end-effector. With $\{\boldsymbol{G}\}$, $\{\boldsymbol{L}'\}$, $\{\boldsymbol{P}'\}$, and $\{\boldsymbol{I}\}$ parallel to each other, angular parameters remain the same when translated within them.

The connection point P can be described under both the base frame and the global frame by rotation matrices and translation vectors as

$$^{\mathrm{B}}\boldsymbol{P} = {}^{\mathrm{B}}\boldsymbol{R}_{\mathrm{P}}\boldsymbol{P} + \boldsymbol{t},$$

and

$$^{\mathrm{G}}\boldsymbol{P} = {}^{\mathrm{G}}\boldsymbol{R}_{\mathrm{B}}({}^{\mathrm{B}}\boldsymbol{P} - \boldsymbol{k}) = {}^{\mathrm{G}}\boldsymbol{R}_{\mathrm{B}}\left({}^{\mathrm{B}}\boldsymbol{R}_{\mathrm{P}}\boldsymbol{P} + \boldsymbol{t} - \boldsymbol{k}\right).$$

The base point B can be also expressed in global frame as

$$^{\mathrm{G}}\boldsymbol{b} = {}^{\mathrm{G}}\boldsymbol{R}_{\mathrm{B}}(\boldsymbol{b} - \boldsymbol{k}).$$

Then the leg vector $\boldsymbol{S}$ (from the origin of the frame L to the origin of the frame U) can be derived from the difference of position vectors $\boldsymbol{P}$ and $\boldsymbol{b}$. Thus, we can get $\boldsymbol{S}$ under the base fame and the global frame, respectively, as

$$^{\mathrm{B}}\boldsymbol{S} = {}^{\mathrm{B}}\boldsymbol{P} - \boldsymbol{b}, \tag{1}$$

and

$$^{\mathrm{G}}\boldsymbol{S} = {}^{\mathrm{G}}\boldsymbol{P} - {}^{\mathrm{G}}\boldsymbol{b} = {}^{\mathrm{G}}\boldsymbol{R}_{\mathrm{B}}({}^{\boldsymbol{B}}\boldsymbol{P} - \boldsymbol{b}). \tag{2}$$

Further, the leg length, which is also the inverse kinematics for the SAS, is given as

$$L = \|{}^{\mathrm{G}}\boldsymbol{S}\| = \|{}^{\mathrm{B}}\boldsymbol{S}\|. \tag{3}$$

The unit leg vector can be described under the base and the global frames, respectively, as

$$^{\mathrm{B}}\boldsymbol{s} = {}^{\mathrm{B}}\boldsymbol{S}/L, \tag{4}$$

and

$$^{\mathrm{G}}\boldsymbol{s} = {}^{\mathrm{G}}\boldsymbol{S}/L = {}^{\mathrm{G}}\boldsymbol{R}_{\mathrm{B}}({}^{\mathrm{B}}\boldsymbol{S}/L) = {}^{\mathrm{G}}\boldsymbol{R}_{\mathrm{B}}{}^{\mathrm{B}}\boldsymbol{s}. \tag{5}$$

The velocity mapping function is founded in the global frame by taking the derivative of Eq. (2) with respect to time, i.e.,

$${}^{\mathrm{G}}\dot{\boldsymbol{S}} = {}^{\mathrm{G}}\boldsymbol{\omega}_{\mathrm{B}} \times {}^{\mathrm{G}}\boldsymbol{R}_{\mathrm{B}}({}^{\mathrm{B}}\boldsymbol{R}_{\mathrm{P}}\boldsymbol{P} + \boldsymbol{t} - \boldsymbol{b}) + {}^{\mathrm{G}}\boldsymbol{R}_{\mathrm{B}}({}^{\mathrm{B}}\boldsymbol{\omega}_{\mathrm{P}} \times {}^{\mathrm{B}}\boldsymbol{R}_{\mathrm{P}}\boldsymbol{P} + \dot{\boldsymbol{t}}).$$

Simplifying, we obtain

$${}^{\mathrm{G}}\dot{\boldsymbol{S}} = {}^{G}\boldsymbol{\omega}_{\mathrm{B}} \times {}^{\mathrm{G}}\boldsymbol{S} + {}^{\mathrm{G}}\boldsymbol{R}_{\mathrm{B}}\,{}^{\mathrm{B}}\dot{\boldsymbol{S}}, \tag{6}$$

where

$${}^{\mathrm{B}}\dot{\boldsymbol{S}} = {}^{\mathrm{B}}\boldsymbol{\omega}_{\mathrm{P}} \times {}^{\mathrm{B}}\boldsymbol{R}_{\mathrm{P}}\boldsymbol{P} + \dot{\boldsymbol{t}}, \tag{7}$$

and ${}^{\mathrm{B}}\dot{\boldsymbol{S}}$ is derived by taking the derivative of Eq. (1) with respect to time.

According to the physical meaning, ${}^{\mathrm{G}}\dot{\boldsymbol{S}}$ can be described in terms of the sliding velocity $\dot{L}$ and the angular velocity of the leg ${}^{\mathrm{G}}\boldsymbol{W}$ under the global frame as

$${}^{\mathrm{G}}\dot{\boldsymbol{S}} = \dot{L}\,{}^{\mathrm{G}}\boldsymbol{s} + L\,{}^{\mathrm{G}}\boldsymbol{W} \times {}^{\mathrm{G}}\boldsymbol{s}. \tag{8}$$

Taking the dot product of the above equation with ${}^{\mathrm{G}}\boldsymbol{s}$, we can obtain

$$\dot{L} = {}^{\mathrm{G}}\boldsymbol{s} \cdot {}^{\mathrm{G}}\dot{\boldsymbol{S}} = {}^{\mathrm{G}}\boldsymbol{s} \cdot \left({}^{\mathrm{G}}\boldsymbol{\omega}_{\mathrm{B}} \times {}^{\mathrm{G}}\boldsymbol{S}\right) + \left({}^{\mathrm{G}}\boldsymbol{R}_{\mathrm{B}}{}^{\mathrm{B}}\boldsymbol{s}\right) \cdot \left({}^{\mathrm{G}}\boldsymbol{R}_{\mathrm{B}}{}^{\mathrm{B}}\dot{\boldsymbol{S}}\right).$$

Simplified with ${}^{\mathrm{G}}\boldsymbol{S} \cdot ({}^{\mathrm{G}}\boldsymbol{\omega}_{\mathrm{B}} \times {}^{\mathrm{G}}\boldsymbol{S}) = 0$, the above equation can be written as

$$\dot{L} = {}^{\mathrm{B}}\boldsymbol{s} \cdot {}^{\mathrm{B}}\dot{\boldsymbol{S}}. \tag{9}$$

Cross-multiplying both sides of Eq. (8) with $\mathbf{s}_{i1}$ gives the angular velocity of the leg as

$${}^{\mathrm{G}}\boldsymbol{W} = {}^{\mathrm{G}}\boldsymbol{s} \times {}^{\mathrm{G}}\dot{\boldsymbol{S}}/L. \tag{10}$$

Similarly, ${}^{\mathrm{G}}\ddot{\boldsymbol{S}}$ can be expressed in two ways. By taking the derivative of Eq. (6) with respect to time, we can obtain

$${}^{\mathrm{G}}\ddot{\boldsymbol{S}} = {}^{\mathrm{G}}\boldsymbol{\varepsilon}_{\mathrm{B}} \times {}^{\mathrm{G}}\boldsymbol{S} + {}^{\mathrm{G}}\boldsymbol{\omega}_{\mathrm{B}} \times {}^{\mathrm{G}}\dot{\boldsymbol{S}} + {}^{\mathrm{G}}\boldsymbol{\omega}_{\mathrm{B}} \times {}^{\mathrm{G}}\boldsymbol{R}_{\mathrm{B}}{}^{\mathrm{B}}\dot{\boldsymbol{S}} + {}^{\mathrm{G}}\boldsymbol{R}_{\mathrm{B}}{}^{\mathrm{B}}\ddot{\boldsymbol{S}}, \tag{11}$$

where

$${}^{\mathrm{B}}\ddot{\boldsymbol{S}} = {}^{\mathrm{B}}\boldsymbol{\varepsilon}_{\mathrm{P}} \times {}^{\mathrm{B}}\boldsymbol{R}_{\mathrm{P}}\boldsymbol{P} + {}^{\mathrm{B}}\boldsymbol{\omega}_{\mathrm{P}} \times ({}^{\mathrm{B}}\boldsymbol{\omega}_{\mathrm{P}} \times {}^{\mathrm{B}}\boldsymbol{R}_{\mathrm{P}}\boldsymbol{P}) + \ddot{\boldsymbol{t}}. \tag{12}$$

Either by taking the derivative of Eq. (7) or according to the physical meaning, ${}^{\mathrm{G}}\ddot{\boldsymbol{S}}$ can be described as

$${}^{\mathrm{G}}\ddot{\boldsymbol{S}} = \ddot{L}\,{}^{\mathrm{G}}\boldsymbol{s} + {}^{\mathrm{G}}\boldsymbol{W} \times ({}^{\mathrm{G}}\boldsymbol{W} \times {}^{\mathrm{G}}\boldsymbol{S}) + 2\,{}^{\mathrm{G}}\boldsymbol{W} \times \dot{L}\,{}^{\mathrm{G}}\boldsymbol{s} + {}^{\mathrm{G}}\boldsymbol{A} \times {}^{\mathrm{G}}\boldsymbol{S}, \tag{13}$$

which may be simplified as

$${}^{\mathrm{G}}\ddot{\boldsymbol{S}} = (\ddot{L} - L\,{}^{\mathrm{G}}\boldsymbol{W} \cdot {}^{\mathrm{G}}\boldsymbol{W})\,{}^{\mathrm{G}}\boldsymbol{s} + 2\,{}^{\mathrm{G}}\boldsymbol{W} \times \dot{L}\,{}^{\mathrm{G}}\boldsymbol{s} + {}^{\mathrm{G}}\boldsymbol{A} \times {}^{\mathrm{G}}\boldsymbol{S}. \tag{14}$$

By taking dot product and cross product at both sides of the above equation with ${}^{\mathrm{G}}\boldsymbol{s}$ separately, we obtain the expression

https://doi.org/10.1017/S0263574711000117 Published online by Cambridge University Press

of the sliding acceleration $\ddot{L}$ and the angular acceleration ${}^{\mathrm{G}}\boldsymbol{A}$ of the leg in the global frame as

$$\ddot{L} = L^{\mathrm{G}}\boldsymbol{W} \cdot {}^{\mathrm{G}}\boldsymbol{W} + {}^{\mathrm{G}}\boldsymbol{s}^{\mathrm{G}}\ddot{\boldsymbol{S}}, \tag{15}$$

and

$${}^{\mathrm{G}}\boldsymbol{A} = ({}^{\mathrm{G}}\boldsymbol{s} \times {}^{\mathrm{G}}\ddot{\boldsymbol{S}} - 2\dot{L}^{\mathrm{G}}\boldsymbol{W})/L. \tag{16}$$

The position vector $\boldsymbol{b}$ is used to get the rotation matrix between the base frame and the local frame L as

$$\begin{array}{ll} x-\text{axis} & \boldsymbol{x} = {}^{\mathrm{B}}\boldsymbol{s}, \\ y-\text{axis} & \boldsymbol{y} = ({}^{\mathrm{B}}\boldsymbol{s} \times \boldsymbol{b})/||{}^{\mathrm{B}}\boldsymbol{s} \times \boldsymbol{b}||, \\ z-\text{axis} & \boldsymbol{z} = \boldsymbol{x} \times \boldsymbol{y}. \end{array}$$

Then, we obtain the rotation matrix as

$$\boldsymbol{T} = [\boldsymbol{x} \quad \boldsymbol{y} \quad \boldsymbol{z}\,].$$

In the second part, the Euler's equation for each leg will be derived around the base point B Therefore, linear accelerations of mass centers of the lower and upper parts in the limb will be expressed related to the base point B too. Conveniently, linear accelerations can be equivalently described under $\{\boldsymbol{L}'\}$, which is attached to the base point B, and parallel to $\{\boldsymbol{G}\}$.

As $\boldsymbol{r}_{\mathrm{Lo}}$ and $\boldsymbol{r}_{\mathrm{Uo}}$ denote position vectors of mass centers of the lower and upper parts in $\{\boldsymbol{L}\}$ and $\{\boldsymbol{U}\}$, the position vectors can be transformed to $\{\boldsymbol{L}'\}$ as

$$\boldsymbol{r}_{\mathrm{L}} = {}^{\mathrm{G}}\boldsymbol{R}_{\mathrm{B}} \cdot \boldsymbol{T}\boldsymbol{r}_{\mathrm{Lo}}, \tag{17}$$

$$\boldsymbol{r}_{\mathrm{U}} = {}^{\mathrm{G}}\boldsymbol{S} + {}^{\mathrm{G}}\boldsymbol{R}_{\mathrm{B}} \cdot \boldsymbol{T}\boldsymbol{r}_{\mathrm{Uo}}. \tag{18}$$

The linear accelerations of mass centers of these two parts in $\{\mathbf{L}'\}$ can be written as

$$\boldsymbol{a}_{\mathrm{L}} = {}^{\mathrm{G}}\boldsymbol{A} \times \boldsymbol{r}_{\mathrm{L}} + {}^{\mathrm{G}}\boldsymbol{W} \times ({}^{\mathrm{G}}\boldsymbol{W} \times \boldsymbol{r}_{\mathrm{L}}), \tag{19}$$

$$\boldsymbol{a}_{\mathrm{U}} = {}^{\mathrm{G}}\boldsymbol{A} \times \boldsymbol{r}_{\mathrm{U}} + {}^{\mathrm{G}}\boldsymbol{W} \times ({}^{\mathrm{G}}\boldsymbol{W} \times \boldsymbol{r}_{\mathrm{U}}) + \ddot{L}^{\mathrm{G}}\boldsymbol{s} + 2^{\mathrm{G}}\boldsymbol{W} \times \dot{L}^{\mathrm{G}}\boldsymbol{s}. \tag{20}$$

The translational acceleration of $\{\boldsymbol{L}'\}$ in $\{\boldsymbol{I}\}$ can be obtained as

$$\boldsymbol{a}_{\mathrm{Lr}} = \boldsymbol{a} + {}^{\mathrm{G}}\boldsymbol{\varepsilon}_{\mathrm{B}} \times {}^{\mathrm{G}}\boldsymbol{b} + {}^{\mathrm{G}}\boldsymbol{\omega}_{\mathrm{B}} \times ({}^{\mathrm{G}}\boldsymbol{\omega}_{\mathrm{B}} \times {}^{\mathrm{G}}\boldsymbol{b}), \tag{21}$$

where $\boldsymbol{a}$ is the linear acceleration vector of the end-effector of the cable-driven Stewart manipulator, and ${}^{\mathrm{G}}\boldsymbol{\varepsilon}_{\mathrm{B}}$ is the angular acceleration vector of the A–B rotator.

The Euler's equation for the SAS end-effector will be derived around the geometrical center o of the end-effector. So the linear acceleration of the mass center of the end-effector will be also expressed related to the geometrical center. Similarly, $\{\boldsymbol{P}'\}$ is introduced, which is attached to the geometrical center o and parallel to $\{\boldsymbol{G}\}$.

As $\boldsymbol{e}_0$ is the position vector of the mass center of the end-effector (including receivers) in the end-effector frame, the vector can be obtained in $\{\boldsymbol{P}'\}$ as

$$\boldsymbol{e} = {}^{\mathrm{G}}\boldsymbol{R}_{\mathrm{B}}{}^{\mathrm{B}}\boldsymbol{R}_{\mathrm{P}}\boldsymbol{e}_0. \tag{22}$$

According to the composite theory of rigid body motion, the angular velocity and acceleration of the end-effector in $\{\boldsymbol{P}'\}$ can be derived as

$${}^{\mathrm{G}}\boldsymbol{\varepsilon}_{\mathrm{P}} = {}^{\mathrm{G}}\boldsymbol{\varepsilon}_{\mathrm{B}} + {}^{\mathrm{G}}\boldsymbol{R}_{\mathrm{B}}{}^{\mathrm{B}}\boldsymbol{\varepsilon}_{\mathrm{P}} + {}^{\mathrm{G}}\boldsymbol{\omega}_{\mathrm{B}} \times ({}^{\mathrm{G}}\boldsymbol{R}_{\mathrm{B}}{}^{\mathrm{B}}\boldsymbol{\omega}_{\mathrm{P}}), \tag{23}$$

$${}^{\mathrm{G}}\boldsymbol{\omega}_{\mathrm{P}} = {}^{\mathrm{G}}\boldsymbol{\omega}_{\mathrm{B}} + {}^{\mathrm{G}}\boldsymbol{R}_{\mathrm{B}}{}^{\mathrm{B}}\boldsymbol{\omega}_{\mathrm{P}}. \tag{24}$$

Then the linear acceleration of the mass center of the end-effector under $\{\boldsymbol{P}'\}$ can be written as

$$\boldsymbol{a}_{\mathrm{P}} = {}^{\mathrm{G}}\boldsymbol{\omega}_{\mathrm{P}} \times ({}^{\mathrm{G}}\boldsymbol{\omega}_{\mathrm{P}} \times \boldsymbol{e}) + {}^{\mathrm{G}}\boldsymbol{\varepsilon}_{\mathrm{P}} \times \boldsymbol{e}. \tag{25}$$

The linear acceleration of $\{\boldsymbol{P}'\}$ relative to $\{\boldsymbol{I}\}$ can be expressed as

$$\boldsymbol{a}_{\mathrm{Pr}} = \boldsymbol{a} + {}^{\mathrm{G}}\boldsymbol{R}_{\mathrm{B}}\ddot{\boldsymbol{t}} + {}^{\mathrm{G}}\boldsymbol{\varepsilon}_{\mathrm{B}} \times \left[{}^{\mathrm{G}}\boldsymbol{R}_{\mathrm{B}}(\boldsymbol{t} - \boldsymbol{k})\right] + {}^{\mathrm{G}}\boldsymbol{\omega}_{\mathrm{B}} \times \left\{{}^{\mathrm{G}}\boldsymbol{\omega}_{\mathrm{B}} \times \left[{}^{\mathrm{G}}\boldsymbol{R}_{\mathrm{B}}(\boldsymbol{t} - \boldsymbol{k})\right]\right\} + 2^{\mathrm{G}}\boldsymbol{\omega}_{\mathrm{B}} \times \left({}^{\mathrm{G}}\boldsymbol{R}_{\mathrm{B}}\dot{\boldsymbol{t}}\right). \tag{26}$$

So far reference points of the Euler equations for each leg and the SAS end-effector have been determined. In addition, all the kinematic and dynamic parameters required in the dynamic equations are determined analytically. In the second part, attention will be paid on the deduction of the inverse dynamic equations of the SAS.

3.2. Dynamics

The moment of inertia $\boldsymbol{I}_{\mathrm{Lo}}$ of the upper part of the leg is defined in $\{\boldsymbol{L}\}$, relative to the mass center. The moment of inertia can be obtained in $\{\boldsymbol{L}'\}$ by rotation matrices as

$$\boldsymbol{I}_{\mathrm{L}} = {}^{\mathrm{G}}\boldsymbol{R}_{\mathrm{B}}\left(\boldsymbol{T}\boldsymbol{I}_{\mathrm{Lo}}\boldsymbol{T}^{\mathrm{T}}\right){}^{\mathrm{G}}\boldsymbol{R}_{\mathrm{B}}^{\mathrm{T}}. \tag{27}$$

Similarly, $\boldsymbol{I}_{\mathrm{Uo}}$ denotes the moment of inertia of the lower part of the leg in $\{\boldsymbol{U}\}$, relative to the mass center. The moment of inertia can be obtained in $\{\boldsymbol{L}'\}$ by rotation matrices as

$$\boldsymbol{I}_{\mathrm{U}} = {}^{\mathrm{G}}\boldsymbol{R}_{\mathrm{B}}\left(\boldsymbol{T}\boldsymbol{I}_{\mathrm{Uo}}\boldsymbol{T}^{\mathrm{T}}\right){}^{\mathrm{G}}\boldsymbol{R}_{\mathrm{B}}^{\mathrm{T}}. \tag{28}$$

In $\{\boldsymbol{L}'\}$, relative to the base point B, the Euler's equation for the entire leg is derived as

$$\begin{aligned} {}^{\mathrm{G}}\boldsymbol{S} \times \boldsymbol{F}_{\mathrm{S}} + \boldsymbol{M}_{\mathrm{U}}{}^{\mathrm{G}}\boldsymbol{s} &= m_{\mathrm{L}}\boldsymbol{r}_{\mathrm{L}} \times \boldsymbol{a}_{\mathrm{L}} + m_{\mathrm{U}}\boldsymbol{r}_{\mathrm{U}} \times \boldsymbol{a}_{\mathrm{U}} \\ &+ (\boldsymbol{I}_{\mathrm{L}} + \boldsymbol{I}_{\mathrm{U}})^{\mathrm{G}}\boldsymbol{A} + {}^{\mathrm{G}}\boldsymbol{W} \times (\boldsymbol{I}_{\mathrm{L}} + \boldsymbol{I}_{\mathrm{U}})^{\mathrm{G}}\boldsymbol{W} \\ &+ (m_{\mathrm{L}}\boldsymbol{r}_{\mathrm{L}} + m_{\mathrm{U}}\boldsymbol{r}_{\mathrm{U}}) \times \boldsymbol{a}_{\mathrm{Lr}} - (m_{\mathrm{L}}\boldsymbol{r}_{\mathrm{L}} + m_{\mathrm{U}}\boldsymbol{r}_{\mathrm{U}}) \times \boldsymbol{g} \end{aligned}$$

where M_{U} is the mode of the constraint moment exerted by the universal joint avoiding rotation along the leg, and $\boldsymbol{F}_{\mathrm{S}}$ is the constraint force of the spherical joints acting on the leg.

The above equation can be simplified as

$${}^{\mathrm{G}}\boldsymbol{S} \times \boldsymbol{F}_{\mathrm{S}} + M_{\mathrm{U}}{}^{\mathrm{G}}\boldsymbol{s} = \boldsymbol{D}, \tag{29}$$

where

$$\begin{aligned} \boldsymbol{D} &= m_{\mathrm{L}}\boldsymbol{r}_{\mathrm{L}} \times \boldsymbol{a}_{\mathrm{L}} + m_{\mathrm{U}}\boldsymbol{r}_{\mathrm{U}} \times \boldsymbol{a}_{\mathrm{U}} + (\boldsymbol{I}_{\mathrm{L}} + \boldsymbol{I}_{\mathrm{U}})^{\mathrm{G}}\boldsymbol{A} + {}^{\mathrm{G}}\boldsymbol{W} \\ &\times (\boldsymbol{I}_{\mathrm{L}} + \boldsymbol{I}_{\mathrm{U}})^{\mathrm{G}}\boldsymbol{W} + (m_{\mathrm{L}}\boldsymbol{r}_{\mathrm{L}} + m_{\mathrm{U}}\boldsymbol{r}_{\mathrm{U}}) \times \boldsymbol{a}_{\mathrm{Lr}} \\ &- (m_{\mathrm{L}}\boldsymbol{r}_{\mathrm{L}} + m_{\mathrm{U}}\boldsymbol{r}_{\mathrm{U}}) \times \boldsymbol{g}. \end{aligned} \tag{30}$$

https://doi.org/10.1017/S0263574711000117 Published online by Cambridge University Press

In order to eliminate M_{U}, taking cross products of both sides of Eq. (29) with unit vector ${}^{\mathrm{G}}\boldsymbol{s}$ leads to

$$ {}^{\mathrm{G}}\boldsymbol{F}_{\mathrm{S}} = \frac{\boldsymbol{D} \times {}^{\mathrm{G}}\boldsymbol{s}}{L} + ({}^{\mathrm{G}}\boldsymbol{s} \cdot {}^{\mathrm{G}}\boldsymbol{F}_{\mathrm{S}}){}^{\mathrm{G}}\boldsymbol{s}. $$

Simplifying, we obtain

$$ {}^{\mathrm{G}}\boldsymbol{F}_{\mathrm{S}} = \boldsymbol{C} + F_{\mathrm{Leg}}{}^{\mathrm{G}}\boldsymbol{s}, \tag{31} $$

where

$$ \boldsymbol{C} = \frac{\boldsymbol{D} \times {}^{\mathrm{G}}\boldsymbol{s}}{L}, \tag{32} $$
$$ {}^{\mathrm{G}}\boldsymbol{s} \cdot {}^{\mathrm{G}}\boldsymbol{F}_{\mathrm{S}} = F_{\mathrm{Leg}}. $$

Now, the vector ${}^{\mathrm{G}}\boldsymbol{F}_{\mathrm{S}}$ is described by a single unknown F_{Leg} in Eq. (31).

The moment of inertia $\boldsymbol{I}_{\mathrm{Po}}$ of the end-effector in $\{\boldsymbol{P}\}$, relative to the mass center, can be transformed to $\{\boldsymbol{P}'\}$ as

$$ \boldsymbol{I}_{\mathrm{P}} = {}^{\mathrm{G}}\boldsymbol{R}_{\mathrm{B}} \left({}^{\mathrm{B}}\boldsymbol{R}_{\mathrm{P}} \boldsymbol{I}_{\mathrm{Po}} {}^{\mathrm{B}}\boldsymbol{R}_{\mathrm{P}}^{\mathrm{T}}\right) {}^{\mathrm{G}}\boldsymbol{R}_{\mathrm{B}}^{\mathrm{T}}. \tag{33} $$

As the reaction force of $({}^{\mathrm{G}}\boldsymbol{F}_{\mathrm{S}})_{\mathrm{i}}$ is exerted on the SAS end-effector, the Newton's equation for the end-effector can be written as

$$ m_{\mathrm{P}}\boldsymbol{g} - \sum_{\mathrm{i}=1}^{6} ({}^{\mathrm{G}}\boldsymbol{F}_{\mathrm{S}})_{\mathrm{i}} - m_{\mathrm{P}}\boldsymbol{a}_{\mathrm{Pr}} = m_{\mathrm{P}}\boldsymbol{a}_{\mathrm{P}}. \tag{34} $$

Substituting $({}^{\mathrm{G}}\mathbf{F}_{\mathrm{S}})_{\mathrm{i}}$ with Eq. (31) results in

$$ \sum_{\mathrm{i}=1}^{6} (F_{\mathrm{Leg}})_{\mathrm{i}}{}^{\mathrm{G}}\boldsymbol{s}_{\mathrm{i}} = m_{\mathrm{P}}\boldsymbol{g} - \sum_{\mathrm{i}=1}^{6} \boldsymbol{C}_{\mathrm{i}} - m_{\mathrm{P}}\boldsymbol{a}_{\mathrm{Pr}} - m_{\mathrm{P}}\boldsymbol{a}_{\mathrm{P}}. $$

Relative to the geometric center o, Euler's equation for the SAS end-effector can be written as

$$ m_{\mathrm{P}}{}^{\mathrm{G}}\boldsymbol{e} \times \boldsymbol{g} - \sum_{\mathrm{i}=1}^{6} {}^{\mathrm{G}}\boldsymbol{R}_{\mathrm{B}}{}^{\mathrm{B}}\boldsymbol{R}_{\mathrm{P}}\boldsymbol{P}_{\mathrm{i}} \times ({}^{\mathrm{G}}\boldsymbol{F}_{\mathrm{S}})_{\mathrm{i}} - m_{\mathrm{P}}{}^{\mathrm{G}}\boldsymbol{e} \times \boldsymbol{a}_{\mathrm{Pr}} $$
$$ = m_{\mathrm{P}}{}^{\mathrm{G}}\boldsymbol{e} \times \boldsymbol{a}_{\mathrm{P}} + {}^{\mathrm{G}}\boldsymbol{\varepsilon}_{\mathrm{P}}\boldsymbol{I}_{\mathrm{P}} + {}^{\mathrm{G}}\boldsymbol{\omega}_{\mathrm{p}} \times (\boldsymbol{I}_{\mathrm{P}}{}^{\mathrm{G}}\boldsymbol{\omega}_{\mathrm{P}}). \tag{35} $$

Substituting $({}^{\mathrm{G}}\boldsymbol{F}_{\mathrm{S}})_{\mathrm{i}}$ with Eq. (31) gives

$$ m_{\mathrm{P}}\,{}^{\mathrm{G}}\boldsymbol{e} \times (\boldsymbol{g} - \boldsymbol{a}_{\mathrm{P}} - \boldsymbol{a}_{\mathrm{pr}}) - {}^{\mathrm{G}}\boldsymbol{\varepsilon}_{\mathrm{P}}\boldsymbol{I}_{\mathrm{P}} - {}^{\mathrm{G}}\boldsymbol{\omega}_{\mathrm{P}} \times (\boldsymbol{I}_{\mathrm{P}}\,{}^{\mathrm{G}}\boldsymbol{\omega}_{\mathrm{P}}) $$
$$ - \sum_{\mathrm{i}=1}^{6} {}^{\mathrm{G}}\boldsymbol{R}_{\mathrm{B}}\,{}^{\mathrm{B}}\boldsymbol{R}_{\mathrm{P}}\boldsymbol{P}_{\mathrm{i}} \times \boldsymbol{C}_{\mathrm{i}} = \sum_{\mathrm{i}=1}^{6} {}^{\mathrm{G}}\boldsymbol{R}_{\mathrm{B}}\,{}^{\mathrm{B}}\boldsymbol{R}_{\mathrm{P}}\boldsymbol{P}_{\mathrm{i}} \times (F_{\mathrm{Leg}})_{\mathrm{i}}{}^{\mathrm{G}}\boldsymbol{s}_{\mathrm{i}}. $$

There are six unknown $(F_{\mathrm{Leg}})_{\mathrm{i}}$ and six linear equations. Thus, $(F_{\mathrm{Leg}})_{\mathrm{i}}$ can be solved from the Newton and Euler equations listed above. Organizing the equations in matrix form, we obtain

$$ \boldsymbol{H}\boldsymbol{F}_{\mathrm{Leg}} = \boldsymbol{N}, \tag{36} $$

where

$$ \boldsymbol{H} = \begin{bmatrix} {}^{\mathrm{G}}\boldsymbol{s}_1 & {}^{\mathrm{G}}\boldsymbol{s}_2 & {}^{\mathrm{G}}\boldsymbol{s}_3 & {}^{\mathrm{G}}\boldsymbol{s}_4 & {}^{\mathrm{G}}\boldsymbol{s}_5 & {}^{\mathrm{G}}\boldsymbol{s}_6 \\ \boldsymbol{j}_1 & \boldsymbol{j}_2 & \boldsymbol{j}_3 & \boldsymbol{j}_4 & \boldsymbol{j}_5 & \boldsymbol{j}_6 \end{bmatrix}, $$
$$ \boldsymbol{j}_i = {}^{\mathrm{G}}\boldsymbol{R}_{\mathrm{B}}\,{}^{\mathrm{B}}\boldsymbol{R}_{\mathrm{P}}\boldsymbol{P}_i \times {}^{\mathrm{G}}\boldsymbol{s}_{\mathrm{i}} \quad i = 1, 2, \ldots 6, $$
$$ \boldsymbol{F}_{\mathrm{Leg}} = [(F_{\mathrm{Leg}})_1\ (F_{\mathrm{Leg}})_2\ (F_{\mathrm{Leg}})_3\ (F_{\mathrm{Leg}})_4\ (F_{\mathrm{Leg}})_5\ (F_{\mathrm{Leg}})_6]^{\mathrm{T}}, $$
$$ \boldsymbol{N} = \begin{bmatrix} \boldsymbol{n}_1 \\ \boldsymbol{n}_2 \end{bmatrix}, $$
$$ \boldsymbol{n}_1 = m_{\mathrm{P}}\boldsymbol{g} - \sum_{\mathrm{i}=1}^{6} \boldsymbol{C}_{\mathrm{i}} - m_{\mathrm{P}}\boldsymbol{a}_{\mathrm{Pr}} - m_{\mathrm{P}}\boldsymbol{a}_{\mathrm{P}}, \tag{37} $$

$$ \boldsymbol{n}_2 = m_{\mathrm{P}}{}^{\mathrm{G}}\boldsymbol{e} \times (\boldsymbol{g} - \boldsymbol{a}_{\mathrm{P}} - \boldsymbol{a}_{\mathrm{Pr}}) - {}^{\mathrm{G}}\boldsymbol{\varepsilon}_{\mathrm{P}}\boldsymbol{I}_{\mathrm{P}} - \sum_{\mathrm{i}=1}^{6} {}^{\mathrm{G}}\boldsymbol{R}_{\mathrm{B}}{}^{\mathrm{B}}\boldsymbol{R}_{\mathrm{P}}\boldsymbol{P}_{\mathrm{i}} $$
$$ \times \boldsymbol{C}_{\mathrm{i}} - {}^{\mathrm{G}}\boldsymbol{\omega}_{\mathrm{P}} \times (\boldsymbol{I}_{\mathrm{P}}{}^{\mathrm{G}}\boldsymbol{\omega}_{\mathrm{P}}). \tag{38} $$

Further, Newton's equation of the upper part of the leg gives

$$ {}^{\mathrm{G}}\boldsymbol{F}_{\mathrm{S}} + m_{\mathrm{U}}\boldsymbol{g} - \boldsymbol{F}_{\mathrm{PJ}} = m_{\mathrm{U}}(\boldsymbol{a}_{\mathrm{U}} + \boldsymbol{a}_{\mathrm{Lr}}), $$

where $\boldsymbol{F}_{\mathrm{PJ}}$ is the sum of the driving and constraint forces of prismatic joint of the leg. Since the driving force is along the leg, taking the dot product with the leg unit vector ${}^{\mathrm{G}}\boldsymbol{s}$ gives

$$ F = F_{\mathrm{Leg}} + U, $$

where

$$ F = {}^{\mathrm{G}}\boldsymbol{s} \cdot \boldsymbol{F}_{\mathrm{PJ}}, $$
$$ U = m_{\mathrm{U}}{}^{\mathrm{G}}\boldsymbol{s} \cdot [\boldsymbol{g} - (\boldsymbol{a}_{\mathrm{U}} + \boldsymbol{a}_{\mathrm{Lr}})]. \tag{39} $$

Moreover, F is the driving force of prismatic joint. The required input forces can be determined in matrix form as

$$ \boldsymbol{F} = \boldsymbol{F}_{\mathrm{Leg}} + \boldsymbol{U}, \tag{40} $$

where

$$ \boldsymbol{F} = [F_1, F_2, F_3, F_4, F_5, F_6]^{\mathrm{T}}, $$

and

$$ U = [U_1, U_2, U_3, U_4, U_5, U_6]^{\mathrm{T}}. $$

Now, the inverse dynamic equations of the Stewart manipulator with a moving base are accomplished. Since the SAS is not designed to withstand external force and torque, external force system is not considered in the equations above. However, external torques and forces, which are usually described in inertia coordinate system, can be directly added to Eqs. (34) and (35). In the next section, the simulation procedure of the acquired equations is illustrated in the MATLAB software.

https://doi.org/10.1017/S0263574711000117 Published online by Cambridge University Press

4. Simulation Procedure

In this section, the simulation of the SAS inverse dynamics is implemented in the MATLAB software. The trajectory of the FAST consists of the motion of the SAS described in $\{\boldsymbol{B}\}$ and the motion of the macro robot, i.e., the FSS (the A–B rotator and the cable-driven Stewart manipulator) is expressed under $\{\boldsymbol{I}\}$. Specifically, the trajectory is described by the position vector $\boldsymbol{t}$ and three Euler angles of the SAS end-effector, two Euler angles of the A–B rotator, as well as the linear acceleration $\boldsymbol{a}$ of the cable-driven Stewart manipulator. Once the trajectory is given, the simulation procedure of the inverse dynamics of the SAS in the MATLAB software can be summarized as follows:

(a) Determine rotation matrices ${}^{\mathrm{B}}\boldsymbol{R}_{\mathrm{P}}$ and ${}^{\mathrm{G}}\boldsymbol{R}_{\mathrm{B}}$ by Roll-Pitch-Yaw angles as

$$
{}^{\mathrm{B}}\boldsymbol{R}_{\mathrm{P}} = \boldsymbol{R}(z,\phi)\boldsymbol{R}(y,\theta)\boldsymbol{R}(x,\psi),
$$

$$
{}^{\mathrm{G}}\boldsymbol{R}_{\mathrm{B}} = \boldsymbol{R}(x,\xi_A)\boldsymbol{R}(y,\xi_B).
$$

where ψ, θ, and ϕ are rotation angles of the SAS end-effector relative to $\{\boldsymbol{B}\}$ around fixed axes. ξ_{A} and ξ_{B} are rotation angles of the A–B rotator in $\{\boldsymbol{G}\}$. After expansion, ${}^{\mathrm{B}}\boldsymbol{R}_{\mathrm{P}}$ and ${}^{\mathrm{G}}\boldsymbol{R}_{\mathrm{B}}$ can be described in detail as

$$
{}^{\mathrm{B}}\boldsymbol{R}_{\mathrm{P}} = \begin{bmatrix} c\phi c\theta & c\phi s\theta s\psi - s\phi c\psi & c\phi s\theta c\psi + s\phi s\psi \\ s\phi c\theta & s\phi s\theta s\psi + c\phi c\psi & s\phi s\theta c\psi - c\phi s\psi \\ -s\theta & c\theta s\psi & c\theta c\psi \end{bmatrix},
$$

$$
{}^{\mathrm{G}}\boldsymbol{R}_{\mathrm{B}} = \begin{bmatrix} c\xi_B & 0 & s\xi_B \\ s\xi_A s\xi_B & c\xi_A & -s\xi_A c\theta\xi_B \\ -c\xi_A s\xi_B & s\xi_A & c\xi_A c\xi_B \end{bmatrix},
$$

where c stands for cosine operation, and s stands for sine operation.

(b) The linear velocity and acceleration of the SAS end-effector in $\{\boldsymbol{B}\}$ can be obtained by taking the derivation of $\boldsymbol{t}$ with respect to time. The angular velocity and acceleration of the SAS end-effector can be obtained in the same way. So are the angular velocity and acceleration of the A–B rotator. The linear accelerations of both $\{\boldsymbol{L}'\}$ and $\{\boldsymbol{P}'\}$ described in $\{\boldsymbol{I}\}$ can be calculated using Eqs. (21) and (26).

(c) Using related equations, such as Eqs. (1), (2), (6), (7), (11), and (12), ${}^{\mathrm{G}}\boldsymbol{S}_i$, ${}^{\mathrm{B}}\boldsymbol{S}_i$, ${}^{\mathrm{G}}\dot{\boldsymbol{S}}_i$, ${}^{\mathrm{B}}\dot{\boldsymbol{S}}_i$, ${}^{\mathrm{G}}\ddot{\boldsymbol{S}}_i$, and ${}^{\mathrm{B}}\ddot{\boldsymbol{S}}_i$ of each limb can be calculated.

(d) Adopting Eqs. (9), (10), (15), (16), (19), and (20), the kinematic parameters of each leg in $\{\boldsymbol{L}'\}$ are computed.

(e) For each limb and the SAS end-effector, we can determine their moment of inertia matrices by using Eqs. (27), (28), and (33).

(f) According to Eqs. (30), (32), and (39), the intermediate parameters $\boldsymbol{C}_i$ and U_i of each limb can be specified.

(g) The kinematic parameters of the SAS end-effector in $\{\boldsymbol{P}'\}$ can be derived by Eqs. (23), (24), and (25).

(h) With kinematic parameters of the SAS end-effector and $\boldsymbol{C}_i$ obtained above, the vector $\boldsymbol{N}$ can be figured out, according to Eqs. (35) and (36).

(i) Finally, the driving force vector $\boldsymbol{F}$ of the Stewart manipulator with a moving base can be determined through Eqs. (34) and (38).

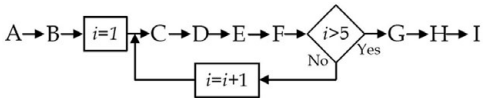


Fig. 5. Flow chart of the inverse dynamic simulation.

Based on the implementation procedure mentioned above, the computer program can be developed to solve the inverse dynamics, using the MATLAB software, as shown in Fig. 5. From steps C to F, all parameters involved belong to an arbitrary limb. Thus, these steps can be implemented by loop statement for six times. The program derived above can only get the driving forces of the SAS at a single moment in the required path. In order to analyze changes of driving forces in an entire trajectory or between a series of continuous states, another programs should be written to discretize the trajectory according to some parameter, such as time, angle, and so on, as well as to call the reverse dynamic program at each discretized point.

5. Driving Force Analysis

As illustrated above, the dynamic formulations for the Stewart manipulator with a moving base have been implemented in the MATLAB software. The emphasis of this section lies in the analysis of the driving forces of the SAS in FAST. The parameters used in the simulation of the SAS are acquired from the FAST prototype designed by the three-dimensional modeling software SolidWorks, and are shown in the Appendix.

According to different physical meanings, there are four factors that affect the driving forces of the SAS, such as the gravity, the motion of the SAS, the motion of the FSS, and the pose of the A–B rotator. Next, analysis will be carried out on these four factors.

5.1. Gravity

In order to analyze the impact of the gravity on the SAS driving forces separately, the SAS can be considered as the Stewart manipulator with a stable base, assuming the FAST is static at the initial state. Then the driving forces introduced by the gravity can be determined individually.

As shown in Fig. 6, the individual driving forces introduced by the gravity are around 1×10^4N. Although limbs of the Stewart manipulator are distributed symmetrically, driving forces of legs are not the same, since of the SAS end-effector's mass and geometric centers are not coincident after receivers are equipped to it.

5.2. Motion of the SAS

The typical trajectory of the SAS is the straight-line motion with high acceleration across the workspace, which is usually described in the base frame for convenience. A planed path is adopted to analyze driving forces of the SAS caused by its motion.

The path of the SAS end-effector is along positive direction of the x'-axis in the base frame without any rotation. The

https://doi.org/10.1017/S0263574711000117 Published online by Cambridge University Press

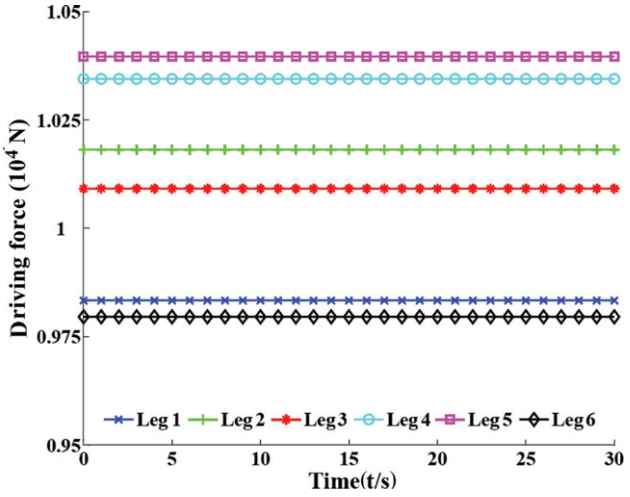


Fig. 6. Static driving forces.

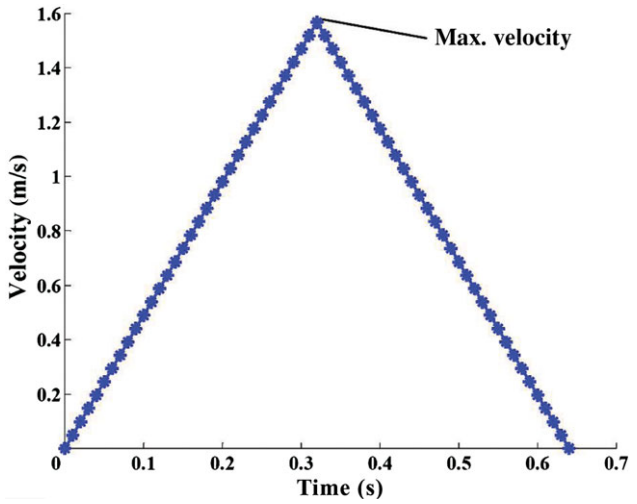


Fig. 7. Velocity curve of the planed path.

trajectory of the SAS end-effector can be expressed as

$$\begin{cases} x' = -0.25 \times 9.8 \times 0.32^2 + 0.25 \times 9.8 \times t^2 & t \le 0.32, \\ x' = 4.9 \times 0.32 \times t - 0.25 \times 9.8 \times t^2 & t > 0.32, \end{cases}$$
$$y' = 0, \ z' = -3.3,$$

where the range of t is from 0 to 0.64 s, determined by the diameter of the workspace. The velocity curve of the path is shown in Fig. 7.

Giving that the FSS is static, rotation angles of the A–B rotator are zero, and the gravity is eliminated, driving forces caused by the SAS motion can be calculated individually. As legs 1, 2, and 3 are symmetrical to legs 4, 5, and 6, respectively, relative to the planed path in $\{\boldsymbol{B}\}$, the SAS driving force curves coincide with each other approximately, as shown in Fig. 8. The driving force range, caused by the SAS motion, is from 1.26×10^4N to -1.06×10^2N.

5.3. Motion of the FSS

Now the limb driving forces resulted from the FSS motion are invested in this section. The motion of the FSS is described in $\{\boldsymbol{I}\}$ for convenience. The maximum linear acceleration of the cable-driven Stewart manipulator is specified as 0.2 m/s^2

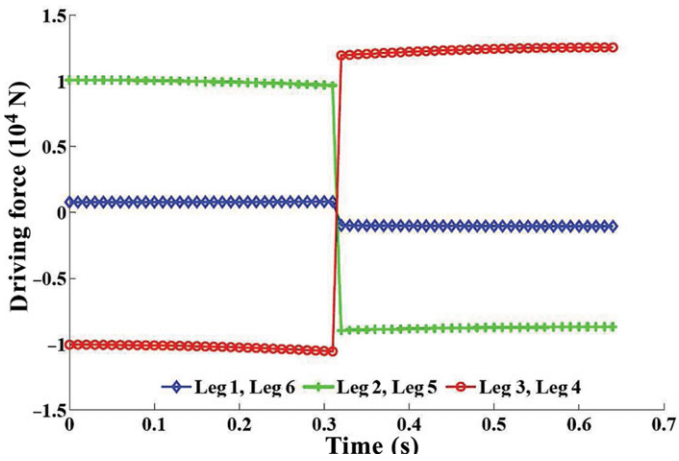


Fig. 8. Driving forces resulted from the SAS motion.

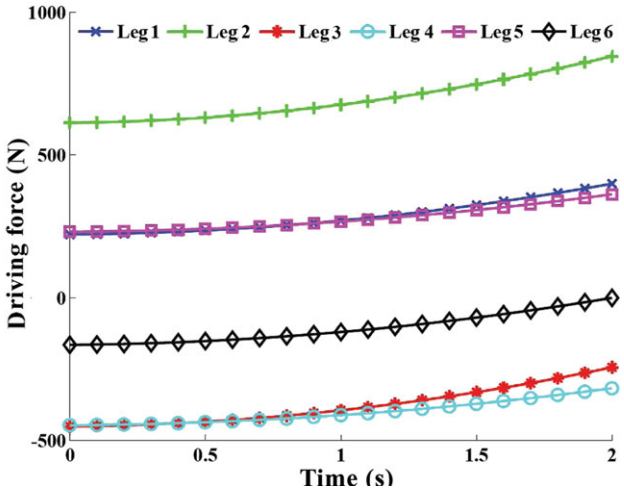


Fig. 9. Driving forces resulted from the FFS motion.

in practice. The maximum angular acceleration of the A–B rotator is 2.5°/s^{2}and the maximum angular velocity is 5°/s. Let's assume that the angular acceleration around the A-axis is 2.5°/s^{2}and the linear acceleration along the X-axis is 0.2 m/s^{2}in $\{\boldsymbol{I}\}$.

In order to eliminate the influence of other factors, it is supposed that the SAS is relative static in the base frame, the whole system is at the initial state, and the rotation angles of the A–B rotator are zero. The motion state of the FSS can be expressed as

$$\begin{cases} \xi_{\mathrm{A}} = 0 \\ \xi_{\mathrm{B}} = 0 \end{cases}, \quad \begin{cases} \xi_{\mathrm{A}} = 0 \\ \xi_{\mathrm{B}} = 0 \end{cases}, \quad \text{and} \quad \begin{cases} \ddot{\xi}_{\mathrm{A}} = 2.5^\circ/\mathrm{s}^2 \\ \ddot{\xi}_{\mathrm{B}} = 0 \end{cases},$$
$$\boldsymbol{a} = [0.2 \text{ m/s}^2, \ 0, \ 0]^{\mathrm{T}}.$$

As shown in Fig. 9, driving forces brought in by the motion of the FSS are determined individually. Since linear and angular accelerations, as well as the angular velocity of the FSS are relatively low, the motion of the FSS has little impact on the driving forces of the SAS in contrast to other factors discussed above. With the review of Eqs. (37)–(39), we find that the linear velocities of the cable-driven Stewart manipulator have nothing to do with the SAS driving forces. The driving force increase, presented

https://doi.org/10.1017/S0263574711000117 Published online by Cambridge University Press

in Fig. 9, is caused by the angular velocity change of the A–B rotator. As the influence of the pose of the A–B rotator cannot be individually determined directly, in the next part, the combined result of all factors is discussed. In addition, the effect of the pose of the A–B rotator can be inferred inversely. In all, the motion of the FSS can be reasonably ignored from the dynamic modeling of the FAST to simplify the procedure of solving the SAS driving forces.

5.4. Combined result

The combined result is obtained by considering the compensation angle of the A–B rotator on the basis of the three factors discussed above. The compensation angle is defined as the angle between the z'-axis of $\{\boldsymbol{B}\}$ and the Z-axis of $\{\boldsymbol{G}\}$. The relationship between rotation angles and the compensation angle can be obtained by the projection of the z'-axis on the Z-axis, and expressed as

$$\cos(\xi_{\mathrm{A}}) \cdot \cos(\xi_{\mathrm{B}}) = \cos(\delta),$$

where ξ_{A} is the rotation angle of the A-axis, ξ_{B} is the rotation angle of the B-axis, and δ is the compensation angle. In order to get the maximum driving forces, let's assume that the A–B rotator works at the maximum compensation angle ($\delta_{\max} = 40^{\circ}$). In order to obtain a complete analysis of the A–B rotator, the rotation angle ξ_{B} can be expressed as

$$\xi_{\mathrm{B}} = \begin{cases} -\arccos(\cos(\delta_{\max})/\cos(\xi_{\mathrm{A}})) \\ \quad (\text{when } \xi_{\mathrm{A}} \text{ changes from } \delta_{\max} \text{ to } -\delta_{\max}) \\ \arccos(\cos(\delta_{\max})/\cos(\xi_{\mathrm{A}})) \\ \quad (\text{when } \xi_{\mathrm{A}} \text{ changes from } -\delta_{\max} \text{ to } -\delta_{\max}) \end{cases},$$

while ξ_{A} changes from $\delta_{\max}$ to $-\delta_{\max}$ and back to $\delta_{\max}$ again at the resolution of 1°. Then the trajectory is a complete cone surface, which is the workspace boundary of the A–B rotator.

At each pose of the A–B rotator, the FSS are kept in extreme motion state (the angular acceleration around the A-axis is $2.5^{\circ}/\mathrm{s}^2$, the linear acceleration along the X-axis is $0.2\ \mathrm{m/s}^2$ in $\{\boldsymbol{I}\}$, the angular velocity around the A-axis is $5^{\circ}/\mathrm{s}$, and the linear velocity along the X-axis is $0.4\ \mathrm{m/s}$ in $\{\boldsymbol{I}\}$) as proposed in Section 5.3, while the SAS tracks the trajectory (straight-line acceleration and deceleration motion) as proposed in Section 5.2. Then the driving force of each SAS limb can be obtained as shown in Fig. 10. The y-ordinate of Fig. 10 represents the rotation angle ξ_{A} around A-axis, and the x-ordinate of Fig. 10 represents time of the SAS straight-line acceleration and deceleration motion. As shown in Fig. 10, the maximum driving force in the combined situation is 3.46×10^4 N approximately.

5.5. Pose of the A–B rotator

In order to estimate the impact of the A–B rotator on the SAS driving forces inversely, the SAS driving forces need to be figured out, considering motions of the SAS and the FSS, as well as the gravity factors. In order to compare with the results acquired above, the planed trajectory is composed of the motion of the SAS and the motion of the FSS as given in Sections 5.2 and 5.3. Then the driving forces of the SAS are calculated as shown in Fig. 11. In addition, the maximum driving force in this motion state is 2.1×10^4 N, and is compared with the combined result as shown in Fig. 12. The impact of the pose of the A–B rotator at maximum compensation angle on the SAS driving forces, estimated inversely, is around 1.36×10^4 N. The impact percentages of these four factors, such as the gravity, the motion of the SAS, the motion of the FSS, and the pose of the A–B rotator, on the maximum driving force of the SAS are determined and shown in Fig. 13.

6. Driving Forces Optimization Strategies

Large driving forces usually mean high-power motors, bulky structure, and extra power consumption, which will dramatically increase system construction and maintenance costs. Thus, the driving forces of the SAS must be optimized and the maximum driving force must be constrained. The available driving force optimization strategies, which provide guidelines for the future optimization, are discussed in this section. As illustrated in Fig. 13, the gravity, the motion of the SAS in $\{\boldsymbol{B}\}$, and the pose of the A–B rotator have most dramatic impacts on the driving forces of the SAS in FAST. Next, these three factors are considered, attempting limit the maximum driving force of the SAS. In order to compare with the result obtained in Section 5.4, the trajectory adopted in this section is the same as the one introduced in Section 5.4, except some parameters.

Owing to the heavy end-effector (including receivers) of the SAS, which is more than 3000 kg in mass, the gravity possesses a dramatic impact on the SAS driving forces. The mass of the end-effector is restrained by mass of receivers attached to it, which have little space for bargaining. However, we can make the geometric center coincide with the mass center of the SAS end-effector by rational arrangement of receivers. Then the driving forces of the SAS in the whole workspace will be homogenized, which will help reduce the maximum driving force. Figure 14 is obtained by calculating the maximum driving force at each pose of the A–B rotator. The optimized curve is obtained by making the mass center coincide with the geometric center in the SAS end-effector, while the reference curve is gotten without the coincidence.

The huge compensation angle of the A–B rotator is also an important factor for large driving force of the SAS. As shown in Fig. 15, the result is acquired on the basis that mass and geometric centers of the SAS end-effector coincide and the maximum compensation angle of the A–B rotator is reduced to 35° ($\delta_{\max} = 35^{\circ}$). Limiting the maximum compensation angle of the A–B rotator is an effective way to reduce the maximum driving force of the SAS. Moreover, it is available. As a 6-DOF parallel manipulator, the Stewart manipulator can easily achieve 10° pitch angle. The 5° pitch angle can be used to compensate the real-time pointing error, while the other 5° pitch angle can be used to relax the A–B rotator's burden of large compensation angle. Thus, the maximum compensation angle of the A–B rotator can be reasonably reduced to 35°. As a result, the maximum driving force of the SAS can be reduced by more than 1000 N. However, the reasonable maximum compensation angle of the A–B rotator still needs to be analyzed further.

Another important factor for the driving forces is the motion of the SAS. In FAST, the SAS is designed to

https://doi.org/10.1017/S0263574711000117 Published online by Cambridge University Press

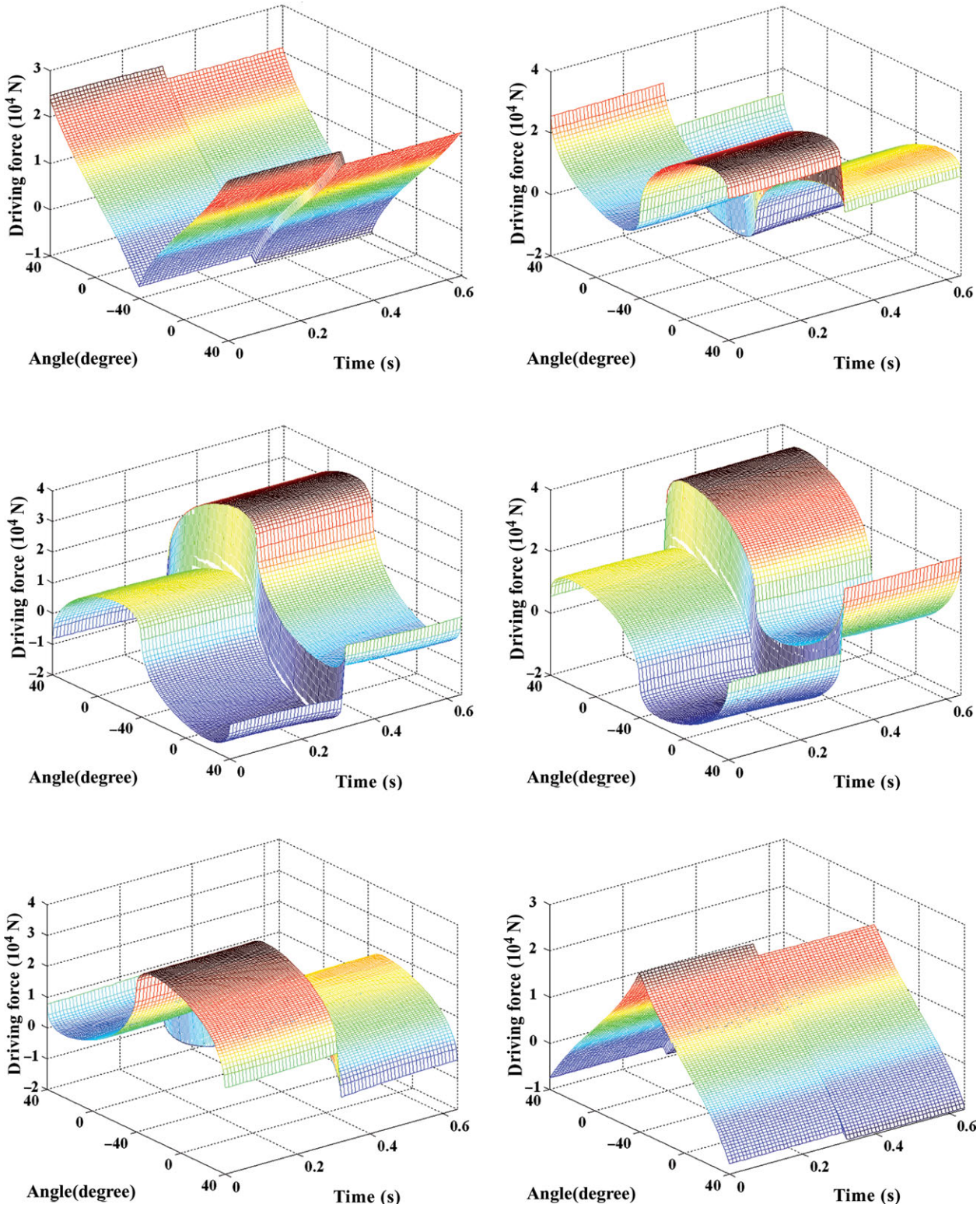


Fig. 10. Driving forces resulted from combined factors. (a) Driving force of leg 1. (b) Driving force of leg 2. (c) Driving force of leg 3. (d) Driving force of leg 4. (e) Driving force of leg 5. (f) Driving force of leg 6.

compensate the real-time following error introduced by cable vibration and wind disturbance. The vibration frequency of the cable-driven Stewart manipulator is about 0.2 Hz, while the wind disturbance frequency is around 0.3 Hz. Given a lower linear acceleration instead of 0.5 g, 3 m/s^2 for example, the reciprocating frequency of the SAS becomes 0.625 Hz, which seems still good enough to meet the terminal precision needs. With a lower linear acceleration, the maximum driving force of the SAS can be reduced a lot. Figure 16 is acquired on the condition that mass and geometric centers of the SAS end-effector coincide and the maximum compensation angle of the A–B rotator is 35°. As illustrated in the figure, the maximum driving force lessens gradually with the decrease of the SAS linear acceleration. Further analysis

https://doi.org/10.1017/S0263574711000117 Published online by Cambridge University Press

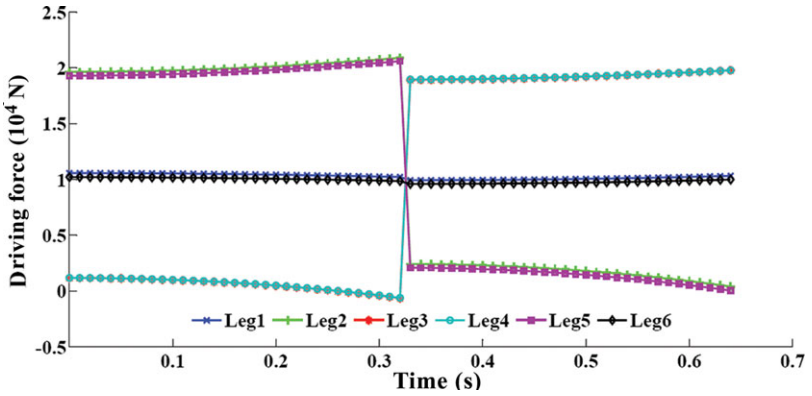


Fig. 11. Driving forces considering motions of the SAS and the FSS, as well as the gravity.

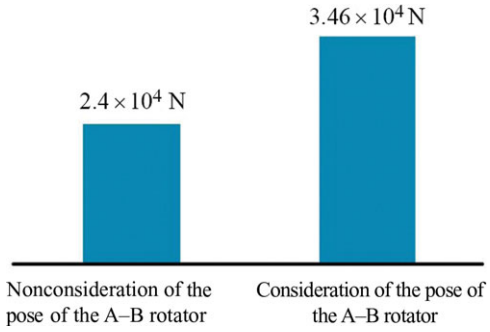


Fig. 12. Maximum driving force comparison of the SAS.

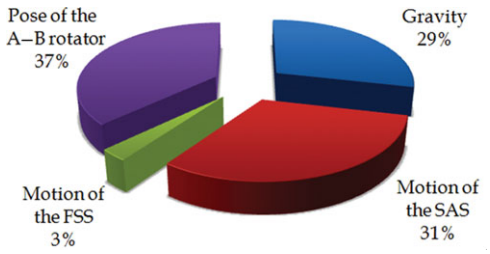


Fig. 13. Contribution ratio of four factors on the maximum driving force of the SAS.

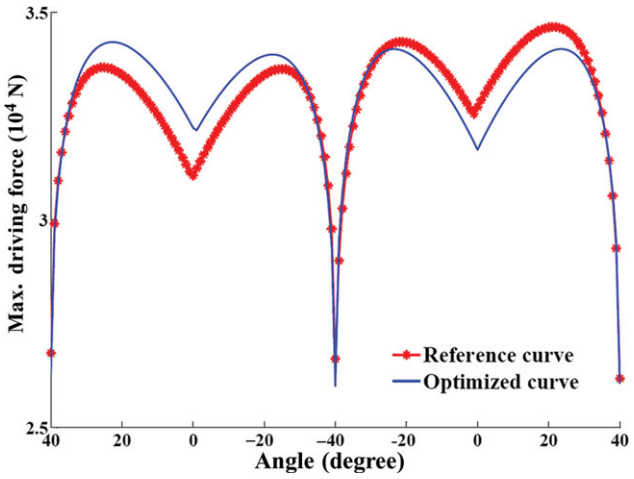


Fig. 14. Optimized results considering the coincidence of mass and geometric centers of the SAS end-effector.

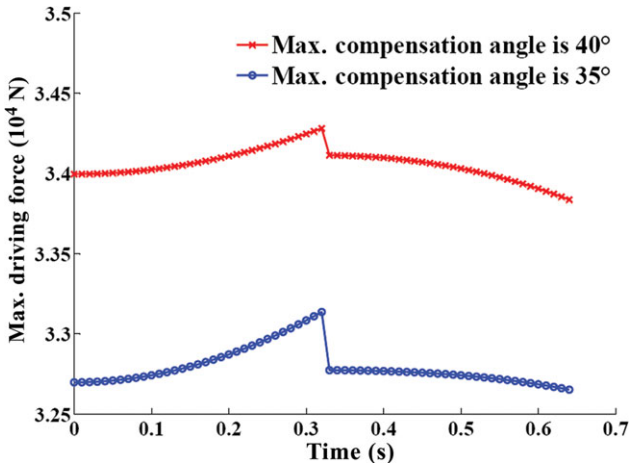


Fig. 15. Optimized results considering the maximum compensation angle of the A–B rotator.

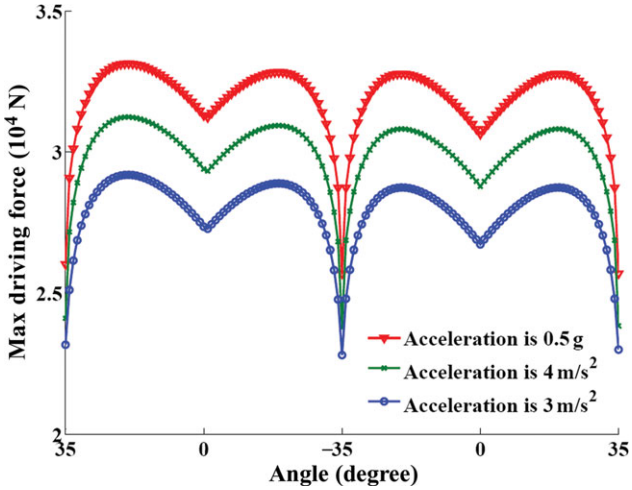


Fig. 16. Optimized results considering the linear acceleration of the SAS.

of the compensation frequency is still required to determine a reasonable maximum linear acceleration of the end-effector for the SAS, balancing needs of both limiting driving forces and maintaining accuracy.

In all, there are three methods that can be adopted to reduce the maximum driving force of the SAS in FAST. They are listed as follows:

https://doi.org/10.1017/S0263574711000117 Published online by Cambridge University Press

- Make the geometric and mass centers of the SAS end-effector coincide with each other, through rational arrangements of the receivers attached to the end-effector.
- Reduce the maximum linear acceleration of the SAS end-effector, on the condition that the terminal tracking accuracy can be guaranteed.
- Make full use of the pitch angle of the SAS, and limit the maximum compensation angle of the A–B rotator.

As shown in Fig. 16, by adopting the optimization strategies proposed above, driving forces of the SAS decrease significantly. The maximum driving force can be easily reduced to 2.9×10^4 N, which is reduced by almost 17%, comparing to the non-optimized result.

7. Conclusion

By adopting the Newton–Euler method introduced in ref. [14–17], the closed-form dynamic equations of the Stewart manipulator with a moving base have been derived. As the motion and pose of the base are considered, the inverse dynamics derived in the paper possesses an inherent wider range of application, and lays the foundation for dynamic analysis of the parallel manipulator with a moving base.

The analysis is carried out on the FAST prototype. According to the features of the FAST, the inverse dynamic model of the SAS can be dramatically simplified by reasonably ignoring the motion of the first support system. The main factors that affect the driving forces of the SAS are the gravity, the motion of the SAS, and the pose of the A–B rotator. As the mass of the SAS end-effector is restricted by the receivers attached to it, only the motion of the SAS and the pose of the A–B rotator are available to optimize the driving forces of the SAS. The optimization attempt reduces the maximum driving force of the SAS by almost 17%. The driving force analysis here is the basis for the servomotor selection, dynamic performance check, and control of the SAS.

Acknowledgments

This research is sponsored by the National Natural Science Foundation of China (Nos. 50605035 and 50975149), the National 973 Program of China (No. 2007CB714007), and the Important National Science & Technology Specific Projects of China (No. 2009ZX04001-042-02).

References

1. R. Nan and B. Peng, "A Chinese concept for the 1-km 2-radio telescope," *Acta Astronaut.* **46**(10–12), 667–675 (2000).
2. R. Nan, "Five hundred meter aperture spherical radio telescope (FAST)," *Sci. China: Series G Phys. Mech. & Astron.* **49**(2), 129–148 (2006).
3. A. Sharon, The Macro/Micro Manipulator: An Improved Architecture for Robot Control, *Ph.D. Thesis* (Massachusetts, USA: Massachusetts Institute of Technology, 1988).
4. J. Lin, "Computer-aided symbolic dynamic modeling for Stewart-platform manipulator," *Robotica* **27**(3), 331–341 (2009).
5. S.-H. Lee, J.-B. Song, W.-C. Choi and D. Hong, "Position control of a Stewart platform using inverse dynamics control with approximate dynamics," *Mechatronics* **13**(6), 605–619 (2003).
6. J. Wu, J. Wang, L. Wang and T. Li, "Dynamics and control of a planar 3-DOF parallel manipulator with actuation redundancy," *Mech. Mach. Theory* **44**(4), 835–849 (2009).
7. D. S. Wu and H. B. Gu, "Adaptive sliding control of six-DOF flight simulator motion platform," *Chin. J. Aeronaut.* **20**(5), 425–433 (2007).
8. B. Dasgupta and T. S. Mruthyunjaya, "The Stewart manipulator: A review," *Mech. Mach. Theory* **35**(2), 15–40 (2000).
9. M. Mahboubkhah, M. J. Nategh and S. E.Khadem, "Vibration analysis of Machine tool's hexapod table," *Int. J. Adv. Manuf. Technol.* **38**(11–12), 1236–1243 (2008).
10. J. Wang, T. Li and G. Duan, "Research and development in the field of parallel kinematic machines" (in Chinese), *Eng. Sci.* **4**(6), 63–70 (2002).
11. X.-J. Liu and L. A. Bonev, "Orientation capability, error analysis, and dimensional optimization of two articulated tool heads with parallel kinematics," *J. Manuf. Sci. Eng. – Trans. ASME* **130**(1), 110151–110159 (2008).
12. A. A. Hanieh, Active Isolation and Damping of Vibration via Stewart Platform, *Ph.D. Thesis* (Belgium: ULB University, 2003).
13. G. Zheng and S. H. Leonard, "Six-degree-of-freedom active vibration isolation using a Stewart platform mechanism," *J. Robot. Syst.* **5**(10), 725–744 (1993).
14. W. Q. D. Do and D. C. H. Yang, "Inverse dynamic analysis and simulation of a platform type of robot," *J. Robot. Syst.* **5**(3), 209–227 (1988).
15. Z. Ji, "Study of the Effect of Leg Inertia in Stewart Platforms," *Proceedings of the 1993 IEEE International Conference on Robotics and Automation*, Atlanta, Georgia, USA (May 2–6, 1993) pp. 121–126.
16. B. Dasgupta and T. S. Mruthyunjaya, "Closed-from dynamic equations of the general Stewart platform through the Newton–Euler approach," *Mech. Mach. Theory* **33**(7), 993–1012 (1998).
17. J. Hong and M. Yamamoto, "A calculation method of the reaction force and moment for a Delta-type parallel link robot fixed with a frame," *Robotica* **27**(4), 579–587 (2009).
18. Y. Li and Q. Xu, "Kinematics and inverse dynamics analysis for a general 3-PRS spatial parallel mechanism," *Robotica* **23**(2), 219–229 (2005).
19. J. Wang and C. M. Gosselin, "A new approach for the dynamic analysis of parallel manipulators," *Multibody Syst. Dyn.* **2**(3), 317–334 (1998).
20. H. Abdellatif and B. Heimann, "Computational efficient inverse dynamics of 6-DOF fully parallel manipulators by using the Lagrangian formalism," *Mech. Mach. Theory* **44**(1), 192–207 (2009).
21. S. Staicu, X.-J. Liu and J. Wang, "Inverse dynamics of the HALF parallel manipulator with revolute actuators," *Nonlinear Dyn.* **50**(1–2), 1–12 (2007).
22. S. Staicu, X.-J. Liu and J. Li, "Explicit dynamics equations of the constrained robotic systems," *Nonlinear Dyn.* **58**(1–2), 217–235 (2009).
23. Z. Shao, X. Tang, X. Chen and L. Wang, "Inertia match research of a 3-RRR reconfigurable planar parallel manipulator," *Chin. J. Mech. Eng.* **22**(3), 1–9 (2009).
24. S. Staicu, "Recursive modelling in dynamics of Delta parallel robot," *Robotica* **27**(2), 199–207 (2009).
25. S. Koekebakker, Model Based Control of a Flight Simulator Motion System, *Ph.D. Thesis* (Delft, Netherlands: Delft University of Technology, 2001)
26. Y. Yuan and Y. Li, "Multi-Degree of Freedom Vibration Model for a 3-DOF Hybrid Robot," *Proceedings of 2009 IEEE/ASME International Conference on Advanced Intelligent Mechatronics*, Singapore (July 14–17, 2009).

https://doi.org/10.1017/S0263574711000117 Published online by Cambridge University Press

Appendix

The kinematic and dynamic parameters of the secondary adjustable system used in Section 5 are as follows (default in SI units):

$$\alpha = 30^\circ, \beta = 15^\circ, \mathrm{r} = 2.5, \mathrm{R} = 5.$$

Base points in {**B**}:

$$\boldsymbol{b} = \begin{bmatrix} 2.8284 & 1.0353 & -3.8637 & -3.8637 & 1.0353 & 2.8284 \\ 2.8284 & 3.8637 & 1.0353 & -1.0353 & -3.8637 & -2.8284 \\ 0 & 0 & 0 & 0 & 0 & 0 \end{bmatrix}.$$

End-effector points in {$\boldsymbol{P}$}:

$$\boldsymbol{p} = \begin{bmatrix} 2.4786 & -0.9567 & -1.5219 & -1.5219 & -0.9567 & 2.4786 \\ 0.3263 & 2.3097 & 1.9834 & -1.9834 & -2.3097 & -0.3263 \\ 0.5040 & 0.5040 & 0.5040 & 0.5040 & 0.5040 & 0.5040 \end{bmatrix}.$$

Mass center of lower part of each leg in {$\boldsymbol{U}$}:

$$\boldsymbol{r}_{\mathrm{U}o} = [1.9909, 0, 0]^{\mathrm{T}}.$$

Mass center of upper part of each leg in {$\boldsymbol{L}$}:

$$\boldsymbol{r}_{\mathrm{Lo}} = [-1, 0, 0]^{\mathrm{T}}.$$

Mass of lower and upper parts of each leg:

$$m_{\mathrm{L}} = 461.16613 \text{ and } m_{\mathrm{U}} = 44.10796.$$

Position of the intersection of the A–B rotator in base frame:

$$\boldsymbol{k} = [0 \quad 0 \quad -1.25]^{\mathrm{T}}.$$

Moment of inertia of lower part of each leg in {$\boldsymbol{U}$}:

$$\boldsymbol{I}_{\mathrm{Uo}} = \begin{bmatrix} 1.83 \times 10^3 & & \\ & 0.67 \times 10^3 & \\ & & 0.67 \times 10^3 \end{bmatrix}.$$

Moment of inertia of upper part of each leg in {$\boldsymbol{L}$}:

$$\boldsymbol{I}_{\mathrm{Lo}} = \begin{bmatrix} 44.20 & & \\ & 58.86 & \\ & & 58.86 \end{bmatrix}.$$

Mass of the SAS end-effector:

$$m_{\mathrm{P}} = 3698.04273.$$

Gravity vector:

$$g = [0 \quad 0 \quad -9.80665]^{\mathrm{T}}.$$

Mass center of the end-effector in {$\boldsymbol{P}$}:

$$\boldsymbol{e}_0 = \begin{bmatrix} -0.04369 & -0.02018 & -0.25225 \end{bmatrix}^{\mathrm{T}}.$$

Moment of inertia of the end-effector in {$\boldsymbol{P}$}:

$$\boldsymbol{I}_{\mathrm{Po}} = \begin{bmatrix} 7.86 \times 10^3 & -1.21 \times 10^2 & -12.13 \\ -1.21 \times 10^2 & 7.76 \times 10^3 & -18.88 \\ -12.13 & -18.88 & 1.412 \times 10^4 \end{bmatrix}.$$

https://doi.org/10.1017/S0263574711000117 Published online by Cambridge University Press